

1 The effect of temperature and humidity on the stability 2 of SARS-CoV-2 and other enveloped viruses

3 Dylan H. Morris^{1*}, Kwe Claude Yinda^{2*}, Amandine Gamble^{3*}, Fernando W. Rossine¹, Qishen Huang⁴,
4 Trenton Bushmaker^{2,5}, Robert J. Fischer², M. Jeremiah Matson^{2,6}, Neeltje van Doremalen², Peter J.
5 Vikesland⁴, Linsey C. Marr⁴, Vincent J. Munster², and James O. Lloyd-Smith³

6 ¹*Department of Ecology & Evolutionary Biology, Princeton University, NJ, USA*

7 ²*National Institute of Allergy and Infectious Diseases, Hamilton, MT, USA*

8 ³*Department of Ecology & Evolutionary Biology, University of California, Los Angeles, CA, USA*

9 ⁴*Department of Civil and Environmental Engineering, Virginia Tech, Blacksburg, VA, USA*

10 ⁵*Department of Microbiology and Immunology, Montana State University, Bozeman, MT, USA*

11 ⁶*Joan C. Edwards School of Medicine, Marshall University, Huntington, WV, USA*

12 *these authors contributed equally

13 October 16, 2020

14 Since emerging in late 2019, SARS-CoV-2 has caused a global pandemic, and it
15 may become an endemic human pathogen. Understanding the impact of envi-
16 ronmental conditions on SARS-CoV-2 viability and its transmission potential
17 is crucial to anticipating epidemic dynamics and designing mitigation strate-
18 gies. Ambient temperature and humidity are known to have strong effects on
19 the environmental stability of viruses¹, but there is little data for SARS-CoV-2,
20 and a general quantitative understanding of how temperature and humidity
21 affect virus stability has remained elusive. Here, we characterise the stability
22 of SARS-CoV-2 on an inert surface at a variety of temperature and humidity
23 conditions, and introduce a mechanistic model that enables accurate predic-
24 tion of virus stability in unobserved conditions. We find that SARS-CoV-2
25 survives better at low temperatures and extreme relative humidities; median
26 estimated virus half-life was more than 24 hours at 10 °C and 40 % RH, but
27 approximately an hour and a half at 27 °C and 65 % RH. Our results highlight
28 scenarios of particular transmission risk, and provide a mechanistic explana-

29 **tion for observed superspreading events in cool indoor environments such as**
30 **food processing plants. Moreover, our model predicts observations from other**
31 **human coronaviruses and other studies of SARS-CoV-2, suggesting the exis-**
32 **tence of shared mechanisms that determine environmental stability across a**
33 **number of enveloped viruses.**

34 In order for viruses to transmit from one host to the next, virions must remain viable (infectious)
35 in the period between release from the transmitting host and uptake by the recipient host. Virus
36 environmental stability thus determines the potential for surface (fomite) transmission and for
37 mid-to-long range transmission through the air. Empirical evidence suggests that virus environ-
38 mental stability strongly depends on ambient temperature and humidity; examples among viruses
39 that infect humans include influenza viruses¹, norovirus², human seasonal coronaviruses³, and
40 the zoonotic coronaviruses SARS-CoV-1⁴ and MERS-CoV⁵.

41 Emerging evidence suggests that the novel zoonotic coronavirus SARS-CoV-2—causative agent
42 of the COVID-19 pandemic—also varies in its environmental stability as a function of tempera-
43 ture and humidity^{6,7}, but the joint effect of these two factors remains unclear. Moreover, despite
44 years of research on virus environmental stability, there do not exist mechanistically motivated
45 quantitative models for virus inactivation as a function of both temperature and humidity. This
46 makes it difficult to generalize from any given experiment to unobserved conditions, or to real-
47 world settings. Existing predictive models for the environmental stability of SARS-CoV-2^{6,8}
48 and other viruses⁹ are phenomenological regression models that do not model the underlying
49 biochemical mechanisms of inactivation. This limits both our insight into the underlying process
50 of virus inactivation and our ability to extrapolate reliably to unobserved conditions.

51 We measured the environmental stability of SARS-CoV-2 virions suspended in cell culture
52 medium deposited onto a polypropylene plastic surface at nine environmental conditions: three
53 relative humidities (RH; 40 %, 65 %, and 85 %) at each of three temperatures (10 °C, 22 °C, and
54 27 °C). We chose temperatures to reflect the temperatures encountered outdoors in late winter
55 (10 °C), indoors in climate-controlled environments (22 °C), and outdoors in summer (27 °C),
56 and chose RH values that reflect temperate atmospheric conditions in both winter and summer.

57 We quantified infectious virus titer over time and estimated virus decay rates and corresponding
58 half-lives in each condition using a simple Bayesian regression model (see [Methods](#)). We
59 quantified the evaporation of the suspension medium and compared virus stability during the

60 sample evaporation phase—while substantial water loss was ongoing—to virus stability after
61 a quasi-equilibrium phase was reached—when further evaporation was not evident over the
62 timescale of the experiment.

63 We then created a mechanistic biochemical model of virus decay kinetics, drawing upon existing
64 hypotheses for how temperature and humidity affect the inactivation chemistry of virus particles
65 in microdroplets^{1,10}. We fit this mechanistic model to our SARS-CoV-2 data, and used it to
66 predict observations from other human coronaviruses and other studies of SARS-CoV-2, in
67 addition to unobserved temperature and humidity conditions.

68 **Empirical patterns of virus decay**

69 Our data suggest that SARS-CoV-2 environmental persistence could vary meaningfully across
70 the range of temperatures and humidities individuals encounter in daily life, with posterior
71 median [95 % credible interval] half-lives as long as 27 h [20, 39] (10 °C, 40 % RH) and as short
72 as 1.5 h [1.1, 2.1] (27 °C, 65 % RH) during the quasi-equilibrium phase (Fig. 1a, Extended Data
73 Table 1).

74 Minimal virus decay occurred during the evaporation phase (Fig. 1a, Extended Data Fig. 2), when
75 excess water was present. Estimated half-lives were long but exact values were highly uncertain,
76 as the small amount of absolute virus inactivation during the brief evaporation phases, combined
77 with the noise involved in sampling and titration, limits our inferential capacity. Posterior median
78 evaporation phase half-lives were 42 h [11, 330] at 10 °C, 12 h [4.5, 160] at 22 °C, and 5.8 h
79 [2.1, 130] at 27 °C (Extended Data Table 1).

80 Overall, measured virus decay became markedly faster as temperature increased across all
81 humidities, with decay at 27 °C roughly five to ten times faster than decay at 10 °C. Across
82 temperatures, virus decay exhibited a U-shaped dependence on RH: roughly two to five times
83 faster at 65 % RH than at 40 % and 100 % RH (Fig. 1a).

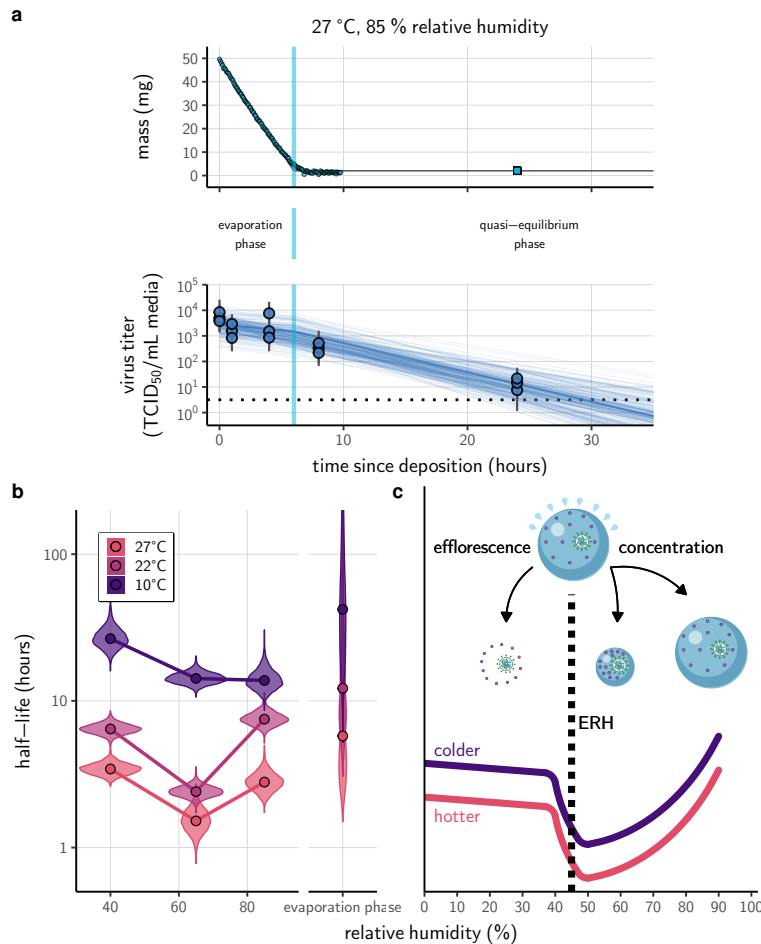


Fig. 1 | Inactivation kinetics and estimated half-life of SARS-CoV-2 on an inert surface as a function of temperature and relative humidity (RH). (a) Example of medium evaporation and virus inactivation as a function of time since deposition; experiments at 27 °C and 85 % shown. Inactivation proceeds in two phases: an evaporation phase during which water mass is lost from the sample to evaporation and a quasi-equilibrium phase once the sample mass has plateaued. Light blue vertical line shows posterior median estimated time that quasi-equilibrium was reached. Top plot: medium evaporation. Dots show measured masses. Square shows measured final (quasi-equilibrium) mass; plotted at 24 h for readability. Lines are 10 random draws from the posterior for the evaporation rate; horizontal section of line reflects the reaching of quasi-equilibrium (measured final mass). Bottom plot: virus inactivation. Points show posterior median estimated titers in $\log_{10} \text{TCID}_{50}/\text{mL}$ for each sample; lines show 95 % credible intervals. Black dotted line shows the approximate single-replicate limit of detection (LOD) of the assay: $10^{0.5} \text{ TCID}_{50}/\text{mL media}$. Three samples collected at each time-point. Lines are 10 random draws per measurement from the posterior distribution for the inactivation rates estimated by the simple regression model (see Methods). (c) Measured virus half-lives. Violin plots show posterior distribution of estimated half-lives, plotted on a logarithmic scale. Dots show posterior median value. Color indicates temperature. Measurements at 40 %, 65 %, and 85 % reflect decay kinetics once the deposited solution has reached quasi-equilibrium with the ambient air. Estimated half-lives for the evaporation phase that occurs prior to quasi-equilibrium are plotted to the right, since conditions during this phase are mainly dilute, and thus analogous to high RH quasi-equilibrium conditions. (b) Schematic of hypothesized effects of temperature and relative humidity on duration of virus viability. Virus half-lives are longer at lower temperatures, regardless of humidity, because inactivation reaction kinetics proceed more slowly. Relative humidity affects virus half-life by determining quasi-equilibrium solute concentration in the droplet containing the virus. Above the efflorescence relative humidity (ERH), solutes are concentrated by evaporation. The lower the ambient humidity, the more water evaporates, the more concentration occurs, and the faster inactivation reactions proceed. Below the ERH, solutes effloresce, forming crystals. Half-lives are thus not particularly sensitive to changes in sub-ERH relative humidity, and half-lives even slightly below the ERH may be substantially longer than half-lives slightly above it.

84 Mechanistic model for temperature and humidity effects

85 Many viruses, including SARS-CoV-2, exhibit exponential decay on surfaces and in aerosols^{1,6,11}.

86 We drew upon known principles of droplet chemistry and its potential effects on virus inactivation
87 chemistry (Fig. 1b) to create a minimal mechanistic model incorporating the effects of both
88 temperature and relative humidity on exponential decay rates.

89 We model temperature dependence with the Arrhenius equation, which describes a reaction rate
90 k as a function of an activation energy E_a , an asymptotic high-temperature reaction rate A , the
91 universal gas constant R , and the absolute temperature T :

$$k = A \exp\left(-\frac{E_a}{RT}\right) \quad (1)$$

92 Prior work has found Arrhenius-like temperature dependence for virus inactivation on surfaces
93 and in aerosols for many viruses¹², including human coronaviruses¹³.

94 Mechanistic principles of virus inactivation as a function of humidity have been more elusive,
95 but recent work has suggested that relative humidity affects virus inactivation by controlling
96 evaporation and thus governing the solute concentrations in a droplet containing virions^{1,10}.
97 In more humid environments, evaporation is slower and some water remains. In less humid
98 environments, evaporation is faster and little or no water remains (Fig. 1b).

99 When released from infected hosts, virions are found in host bodily fluids, whereas viral in-
100 activation experiments are typically conducted in cell culture medium containing amino-acids
101 and electrolytes, in particular sodium chloride (NaCl)^{14,15}. Prior work has found that higher
102 quasi-equilibrium solute concentrations are associated with faster virus inactivation rates^{16,17}.
103 The simplest explanation for this is that the measured solute concentration is a direct proxy for
104 the concentration of the reactants governing the inactivation reaction. Thus ambient humidity
105 affects the reaction rate by setting the quasi-equilibrium concentrations of the reactants that
106 induce inactivation of the virus.

107 The exact quasi-equilibrium state reached will depend on the solutes present, since different
108 solutes depress vapor pressure to different degrees. In electrolyte solutions like bodily fluids or
109 cell culture media, efflorescence is also important. Below a threshold ambient humidity—the
110 efflorescence relative humidity (ERH)—electrolytes effloresce out of solution, forming a crystal

111 (Fig. 1b). For NaCl solutions at standard temperature and pressure, the ERH is around 45 %¹⁸.
112 Below the ERH, inactivation may proceed differently, since the reaction no longer occurs in
113 solution. The notable U-shape of virus inactivation as a function of relative humidity, observed
114 in our data (Fig. 1a) and elsewhere in the literature¹⁶, including for coronaviruses^{19,20}, could be
115 explained by this regime shift around the ERH (Fig. 1b).

116 To quantify these effects, we model virus inactivation at quasi-equilibrium on inert surfaces as
117 a chemical reaction with first-order reaction kinetics; that is, the quantity of virus is the limiting
118 reactant, and the concentrations of other reactants are assumed to be approximately constant
119 over time. At constant temperature and humidity, the quantity of virus should then exhibit
120 exponential decay. During the evaporation phase prior to quasi-equilibrium, reactants are less
121 concentrated and decay is expected to be slower, as observed from our data (Fig. 1a). If small
122 initial droplet sizes are used—as in real-world depositions (predominantly < 10 µL^{21–23}) and in
123 some experiments—evaporative quasi-equilibration should be near instant, and so inactivation
124 should follow the kinetics at quasi-equilibrium. Larger droplets, such as those used in our
125 experiments, will take more time to equilibrate (depending on temperature and humidity),
126 allowing us to distinguish the quasi-equilibrium phase from the evaporation phase.

127 We partition inactivation at quasi-equilibrium into two humidity regimes, solution and efflo-
128 resced, according to whether the ambient RH is above the ERH (solution) or below (effloresced).
129 In either case, we approximate virus inactivation as a first-order reaction with rate k_{sol} or k_{eff} ,
130 respectively. We use an ERH of 45 %, meaning that 40 % experiments are in the effloresced
131 regime and 65 % and 85 % experiments are in the solution regime.

132 We model the inactivation rates k using two Arrhenius equations defined by different activation
133 energies E_a and asymptotic high-temperature reaction rates A . In solution conditions, we further
134 modulate k_{sol} by a quasi-equilibrium “concentration factor” $\frac{[S_{\text{eq}}]}{[S_0]}$: how concentrated the solution
135 has become at quasi-equilibrium $[S_{\text{eq}}]$ relative to its initial state $[S_0]$. Additional details are
136 provided in the Supplementary Information (SI), section 1. Given our assumption of first-order
137 kinetics, an n-fold increase in the non-virion reactant concentrations should translate directly
138 into an n-fold increase in the inactivation rate.

$$k_{\text{eff}} = A_{\text{eff}} \exp \left(-\frac{E_a^{\text{eff}}}{RT} \right) \quad (2)$$

$$k_{\text{sol}} = \frac{[S_{\text{eq}}]}{[S_0]} A_{\text{sol}} \exp\left(-\frac{E_a^{\text{sol}}}{RT}\right) \quad (3)$$

139 We estimated A_{eff} , A_{sol} , E_a^{eff} , and E_a^{sol} from our data, constraining all to be positive. We treated
140 evaporation phase data as governed by k_{sol} , with a dynamic value of the concentration factor
141 $\frac{[S(t)]}{[S_0]}$ (SI section 1.4). We computed the quasi-equilibrium concentration factor $\frac{[S_{\text{eq}}]}{[S_0]}$ in two ways:
142 using measurements from our evaporation experiments (measured concentration fit) and with
143 a theoretically motivated curve fit to our virological data (modeled concentration fit, Extended
144 Data Fig. 8). See SI section 2.5.3 for details.

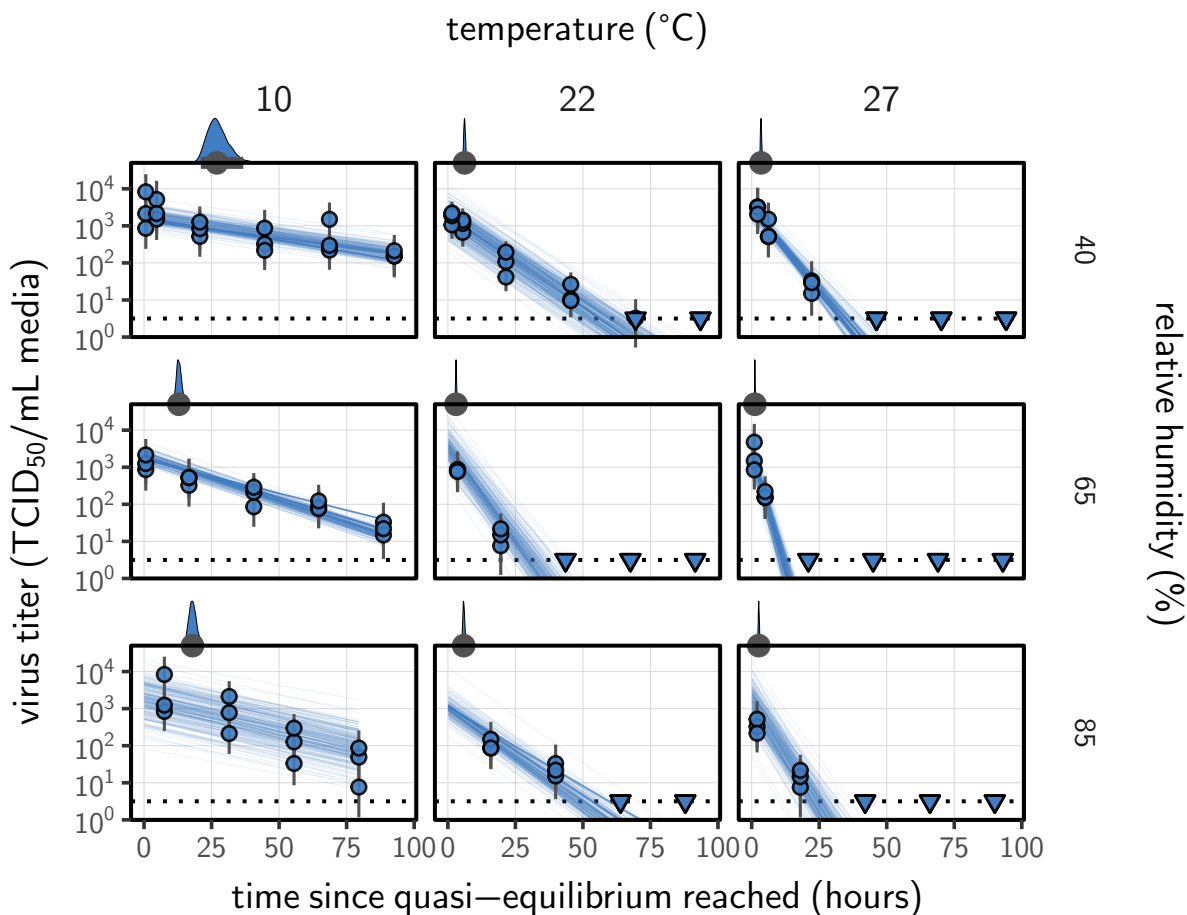


Fig. 2 | Estimated titers and mechanistic model fit for SARS-CoV-2 stability on polypropylene at quasi-equilibrium. Points show posterior median estimated titers in $\log_{10} \text{TCID}_{50}/\text{mL}$ for each sample; lines show 95 % credible intervals. Time-points with no positive wells for any replicate are plotted as triangles at the approximate single-replicate limit of detection (LOD) of the assay—denoted by a black dotted line at $10^{0.5} \text{ TCID}_{50}/\text{mL}$ media—to indicate that a range of sub-LOD values are plausible. Three samples collected at each time-point. x-axis shows time since quasi-equilibrium was reached, as measured in evaporation experiments. Lines are random draws (10 per sample) from the joint posterior distribution of the initial sample virus concentration and the mechanistic model predicted decay rate; the distribution of lines gives an estimate of the uncertainty in the decay rate and the variability of the initial titer for each experiment. Density plots above each box show posterior distribution of virus half-life according to the model for the given condition; point under the density shows the posterior median half-life and line shows a 95 % credible interval. Parameters from the measured concentration model fit.

145 Model fitting and prediction of unobserved conditions

146 Our dataset comprises 9 experimental conditions, each with 7 time-points that span the evap-
147 oration and quasi-equilibrium phases. We sought to explain the virus inactivation rates across
148 this entire dataset using our mechanistic model with just 4 free parameters: the effloresced and
149 solution activation energies E_a^{eff} and E_a^{sol} and the asymptotic high-temperature reaction rates
150 A_{eff} and A_{sol} . The mechanistic function used and the constraint on the parameters to be positive
151 means that inactivation rate must increase with temperature and with increasing solute concen-
152 tration. Remarkably, the fit of the mechanistic model (Fig. 2, Extended Data Figs. 3, 4, 6) is
153 virtually indistinguishable from the fit of the simple regression, which estimates independent
154 exponential decay rates for each condition (Extended Data Figs. 2, 5, see SI section 2.4.1).

155 We used the mechanistic model to predict SARS-CoV-2 half-life for unobserved temperature and
156 humidity conditions from 0 to 40 °C, and from 0 to 100 % RH. We chose these ranges to reflect
157 environments encountered by human beings in daily life. We did not extrapolate to temperatures
158 below 0 °C since inactivation kinetics may be different when fluid containing the virus freezes.
159 The exact freezing points of suspension medium and human fluids at sea level will depend on
160 solute concentration, but will typically be below the 0 °C freezing point of pure water.

161 Median predicted SARS-CoV-2 half-life varies by more than three orders of magnitude, from less
162 than half an hour at 40 °C and 46 % RH (i.e., just above the ERH), to more than a month at 0 °C
163 and 100 % RH (Fig. 3a and c). We find good qualitative agreement between model predictions
164 and model-free estimates from our data, including the long half-lives prior to quasi-equilibrium,
165 and the U-shaped effect of humidity on virus half-life is readily explained by the regime-shift at
166 the ERH (Fig. 3a). In particular, half-lives become extremely long at cold temperatures, and at
167 very high RH (corresponding to low solute concentrations; Fig. 3b).

168 As a stronger test of our model's validity, we used our estimated E_a and A values to make out-
169 of-sample predictions of the half-lives of five human coronaviruses reported from independent
170 studies: four betacoronaviruses (SARS-CoV-2, SARS-CoV-1, MERS-CoV and HCoV-OC43)
171 and one alphacoronavirus (HCoV-229E). We compiled data on the environmental stability of
172 those viruses under conditions ranging from 4 to 95 °C, from 30 to 80 % RH, and on a range
173 of surfaces or bulk media, and computed empirical—model-free—estimates of virus half-lives
174 (Extended Data Tables S1–2).

175 Where both temperature and RH were available, we compared these model-free estimates to

¹⁷⁶ predictions based on the mechanistic model parameterized with our SARS-CoV-2 data (Fig. 3c,
¹⁷⁷ Extended Data Fig. 7). We found striking agreement for half-life estimates both above and below
¹⁷⁸ the ERH, and for temperatures ranging from 4 to 37 °C.

¹⁷⁹ To include a broader range of conditions in our out-of-sample model testing, we used our model
¹⁸⁰ to predict half-lives observed in all comparable studies by extrapolating from a reference half-life
¹⁸¹ in each study. Predicted half-lives matched observations well across five orders of magnitude
¹⁸² (Fig. 3d), despite spanning five virus species and despite important heterogeneities in the data
¹⁸³ collection process (SI section 3). The two conspicuous outliers, where SARS-CoV-2 half-lives
¹⁸⁴ were measured to be substantially shorter than our prediction, correspond to samples exposed
¹⁸⁵ to high heat in closed vials^{24,25} which is known to accelerate virus inactivation²⁶.

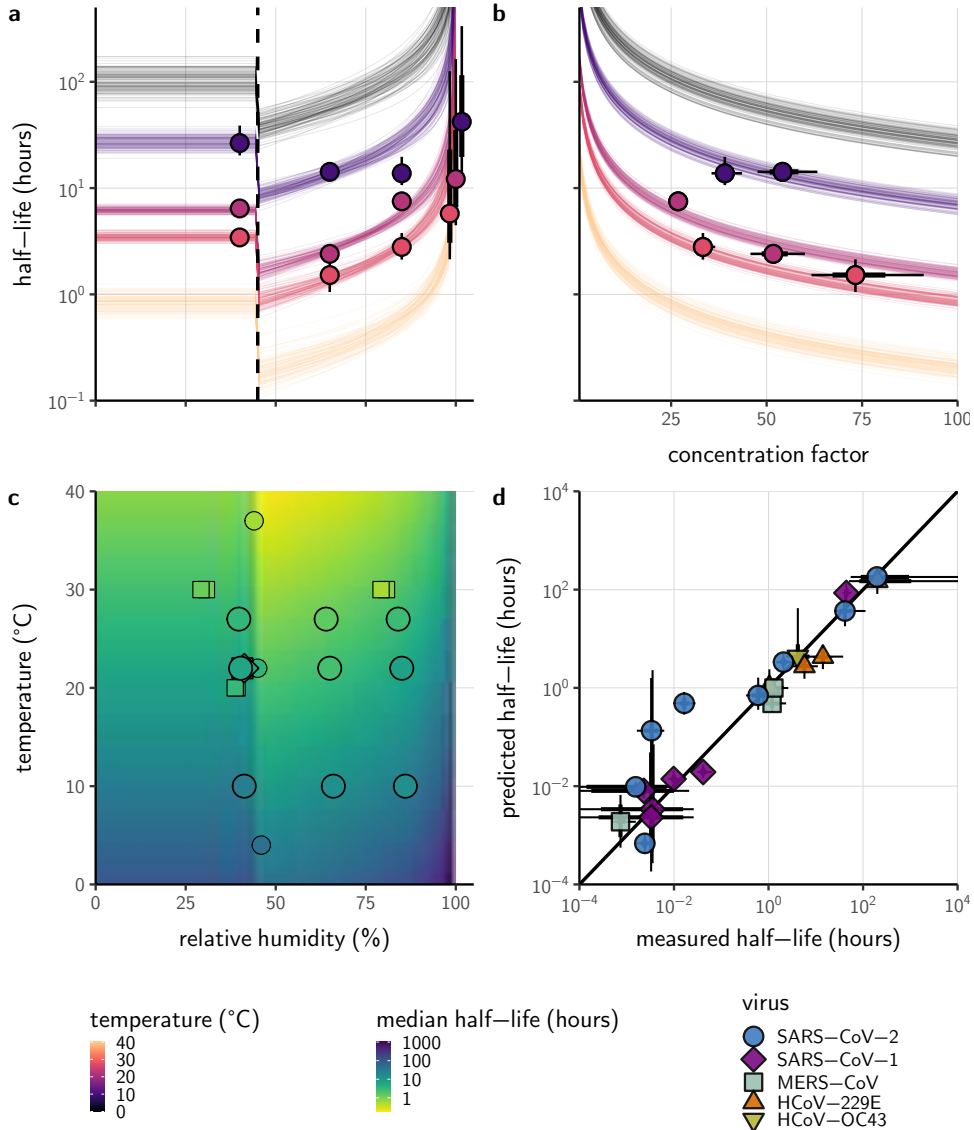


Fig. 3 | Extrapolation of human coronavirus half-life from the mechanistic model to unobserved temperatures and humidities and prediction of data from the literature. (a) Predicted half-life as a function of relative humidity according to the modeled concentration fit. Points show posterior median for measured half-lives, estimated without the mechanistic model (i.e. independent estimation of a fixed exponential decay rate for each temperature/humidity combination), lines show a 68 % (thick) and 95 % (thin) credible interval. Dashed line shows the ERH. Estimated evaporation phase half-lives plotted at the right. Colored lines show predicted half-lives as a function of humidity at five temperatures: 0 $^{\circ}\text{C}$, 10 $^{\circ}\text{C}$, 22 $^{\circ}\text{C}$, 27 $^{\circ}\text{C}$, and 40 $^{\circ}\text{C}$. 100 random draws from the posterior distribution are shown at each temperature to visualize uncertainty. Line and point colors indicate temperature. (b) Predicted half-life above the ERH as a function of quasi-equilibrium concentration factor according to the measured concentration fit. Points and lines as in a, but only solution (above ERH) conditions shown. (c) Heatmap showing posterior median predicted half-lives from the modeled concentration fit as a function of temperature and relative humidity. Posterior median estimated half-lives for human coronaviruses from our study and from the literature plotted on top (see also Extended Data Table 2 and Fig. 7). Shape indicates virus; measurements from our own group are shown slightly larger with a slightly thicker outline. (d) Comparison of model-free estimates (x-axis) to model predictions (y-axis) for human coronavirus half-lives. Points show posterior median for measured (horizontal) or predicted (vertical) half-lives and lines show a 68 % (thick) and 95 % (thin) credible interval. Shape indicates virus; only data from the literature are shown.

186 Discussion

187 Combining novel data, mathematical modelling, and a meta-analysis of existing literature, we
188 have developed a unified, mechanistic framework to quantify the joint effects of temperature
189 and humidity on virus stability. In particular, our model provides a mechanism for the non-
190 linear and non-monotonic relationship between relative humidity and virus stability previously
191 observed^{16,19,20}. Our work documents and explains the strong dependence of SARS-CoV-2
192 stability on environmental temperature and relative humidity, and accurately predicts half-lives
193 for five coronavirus species in conditions from 4 to 95 °C, and from 30 to 80 % RH and in bulk
194 solution.

195 Our findings have direct implications for the epidemiology and control of SARS-CoV-2 and
196 other enveloped viruses. The majority of SARS-CoV-2 clusters have been linked to indoor
197 settings²⁷, suggesting that virus stability in indoor environmental conditions may be an impor-
198 tant determinant of super-spreading risk. Our results provide a mechanistic explanation for
199 the many observed SARS-CoV-2 superspreading events in cool indoor environments such as
200 food processing plants, where the typical temperature is around 10 °C^{28,29}, or in dry indoor
201 environments such as long-distance flights^{30,31}. Conversely, our results imply that the relative
202 rarity of outdoor SARS-CoV-2 transmission clusters is not readily explained by temperature
203 and humidity effects, since these conditions outdoors during temperate winters should be fa-
204 vorable for the virus. Instead, increased dilution of aerosols and UV light inactivation³² may
205 be more important than the effects of temperature and humidity outdoors. In contrast, typical
206 climate-controlled conditions indoors (moderate temperature and low humidity) are favorable
207 for virus stability, and specialized conditions such as those found in food processing plants even
208 more so. Our results highlight the importance of proper personal protective equipment and
209 improved ventilation for protecting workers, particularly in cold indoor settings, and the general
210 transmission risks associated with indoor gatherings.

211 The effects of temperature and humidity we observe in our data and model are relevant to both
212 fomite and airborne transmission. Prior work has shown that virus decay as a function of RH is
213 similar in droplets on surfaces and suspended aerosols^{10,33}. Various studies of smaller deposited
214 droplets³⁴ or aerosols^{3,17,35} have reported similar qualitative patterns to those we observe on
215 an inert surface, with increased decay rates at high temperatures and a U-shaped effect of RH.
216 Furthermore, small particles containing virions can be re-suspended from surfaces by air currents
217 and thus contribute to aerosol transmission³⁶. Re-suspension is further enhanced by procedures

218 such as high-pressure washing, which is common in food processing plants. While the relative
219 contributions of aerosol and fomite transmission to the epidemiology of SARS-CoV-2 remain
220 uncertain^{37,38}, our results indicate that cold situations present elevated transmission risks for
221 either mode, especially if air is either dry or very humid. It has been speculated, for instance,
222 that chilled or frozen foods might allow for rare but impactful long-range fomite transmission³⁹.
223 Our results show that this is conceivable, as there is good empirical and mechanistic support for
224 prolonged virus viability at very low temperatures.

225 Implications for the seasonality of viral transmission are less certain. It is widely speculated
226 that SARS-CoV-2 transmission will be faster in temperate winters^{40,41}, as occurs with other
227 respiratory viruses⁴². Major seasonal or climate-mediated effects on SARS-CoV-2 epidemiology
228 have yet to be demonstrated^{43,44}; this is expected since population susceptibility and epidemic
229 control measures are more important than seasonality in an early pandemic context⁴¹. In the
230 future, climatic conditions are likely to affect SARS-CoV-2 epidemiology, but climatic effects on
231 virus stability may not be the dominant mechanism. While virus survival in cold temperatures is
232 often cited as a potential mechanism for respiratory virus seasonality, this effect is confounded
233 with changes in human behaviour and circannual variation in immunity, among other factors^{42,45}.

234 Our work has implications for the study of virus environmental stability and seasonality more
235 broadly. Whether absolute or relative humidity is more important for influenza stability has been
236 a matter of debate^{1,46}. The answer has proved elusive because it is difficult to disentangle the
237 effects of humidity from those of temperature. Our mechanistic model permits principled dis-
238 aggregation of those effects, and reveals a strong effect of relative humidity even after accounting
239 for the effects of temperature.

240 There may thus exist general principles that govern virus inactivation across enveloped viruses,
241 and even more broadly. Similar empirical patterns of temperature and humidity dependence to
242 what we see for SARS-CoV-2 have been observed for other important enveloped RNA viruses,
243 including influenza viruses, paramyxoviruses, rhabdoviruses and retroviruses^{17,20,34,35,47}, sug-
244 gesting the existence of a shared mechanism. Some enveloped DNA viruses such as her-
245 pesviruses and poxviruses^{20,47} and some encapsulated viruses such as polioviruses^{20,48} also
246 show similar empirical behavior. Experiments have found that heat treatment of viruses reduces
247 infectivity principally by degrading surface proteins⁴⁹, lending further support to a chemical
248 model of environmental virus inactivation. We discuss additional practical implications for the
249 empirical study of virus environmental stability in the SI (section 4).

250 Despite years of research on virus stability as a function of temperature and humidity and
251 plausible hypotheses about the underlying chemistry, proposed mechanisms have lacked explicit
252 quantitative support. By encoding the underlying chemistry into a mathematical model and
253 estimating parameters using modern computational techniques, we provide such support, with
254 critical insights for the control of an ongoing pandemic. Our empirical results provide mechan-
255 nistic insight into transmission risks associated with cold and climate controlled indoor settings,
256 while our modeling work allows for explicit quantitative comparison of the aerosol and fomite
257 risks in different environments, and suggests that simple, robust general mechanisms govern the
258 viability of enveloped viruses: hotter, more concentrated solutions are favorable to chemical
259 reactions—and therefore unfavorable to viruses.

260 **Methods**

261 **Laboratory experiments**

262 **Viruses and titration**

263 We used SARS-CoV-2 strain HCoV-19 nCoV-WA1-2020 (MN985325.1)⁵⁰ for this study. We
264 quantified viable virus by end-point titration on Vero E6 cells as described previously^{11,51}, and
265 inferred posterior distributions for titers and exponential decay rates directly from raw titration
266 data using Bayesian statistical models (see [Statistical analyses and mathematical modelling](#)
267 below).

268 **Virus stability experiment**

269 We measured virus stability on polypropylene (ePlastics, reference PRONAT.030X24X47S/M)
270 as previously described¹¹. We prepared a solution of Dulbecco's Modified Eagle Medium
271 (DMEM, a common cell culture medium) supplemented with 2 mM L-glutamine, 2 % fetal
272 bovine serum and 100 units/mL penicillin/streptomycin, and containing 10^5 TCID₅₀/mL SARS-
273 CoV-2. Polypropylene disks were autoclaved for decontamination prior to the experiment. We
274 then placed 50 μ L aliquots of this SARS-CoV-2 suspension onto the polypropylene disks under
275 nine environmental conditions: three RH (40 %, 65 %, and 85 %) at each of three temperatures
276 (10 °C, 22 °C, and 27 °C). These controlled environmental conditions were produced in incubators
277 (MMM Group CLIMACELL and Caron model 6040) with protection from UV-B or UV-C

278 exposure. We prepared 216 disks corresponding to three replicates per eight post-deposition
279 time-points (0, 1, 4, 8, and 24 hours, then daily for 4 days) for the nine conditions. At each
280 time-point, samples were collected by rinsing the disks with 1 mL of DMEM and stored at
281 -80°C until titration.

282 **Evaporation experiment**

283 We measured the evaporation kinetics of suspension medium under the same temperature and hu-
284 midity conditions as the virus stability experiments. We placed 50 μL aliquots of supplemented
285 DMEM onto polypropylene disks in a Electro-Tech Systems 5518 environmental chamber. The
286 polypropylene disks were rinsed three times 1M sulfuric acid, ethanol and DI H₂O respec-
287 tively before use. We measured medium mass $m(t)$ every 5 min for up to 20 h or until a
288 quasi-equilibrium was reached using a micro-balance (Sartorius MSE3.6P-000-DM, readability
289 0.0010 mg). The chamber of the micro-balance was half-opened to keep air circulating with the
290 environmental chamber. The flow entering the balance chamber decreased the balance accuracy
291 to around 0.010 mg. We measured initial droplet mass ($m(0)$) and final droplet mass ($m(\infty)$)
292 under closed-chamber conditions to increase accuracy.

293 **Statistical analyses and mathematical modelling**

294 We quantified the stability of SARS-CoV-2 under different conditions by estimating the decay
295 rates of viable virus titers. We inferred individual titers using a Bayesian model we have
296 previously described²⁶. Briefly, the model treats titration well infection as a Poisson single-hit
297 process. We inferred raw exponential decay rates by modifying a previously-described simple
298 regression model²⁶ to account for the evaporation phase. See the SI (section 2.4) for model
299 description.

300 We estimated parameters of our mechanistic models by predicting titers based on those models
301 and then applying the same Poisson single-hit observation process to estimate parameters from
302 the data. See the SI (section 2.5) for a complete description, including model priors.

303 We estimated evaporation rates and corresponding drying times by modeling mass loss for each
304 environmental condition i as linear in time at a rate β_i until the final mass $m(\infty)$ was reached,
305 See the SI (sections 1.2, 2.3) for a full description including model priors.

306 We drew posterior samples using Stan⁵², which implements a No-U-Turn Sampler (a form of

307 Markov Chain Monte Carlo), via its R interface RStan⁵³.

308 **Meta-analysis**

309 To test the validity of our model beyond the measured environmental conditions (i.e., beyond 10–
310 27 °C and 40–85 % RH), we compiled data from 11 published studies on human coronaviruses,
311 including SARS-CoV-2, SARS-CoV-1, MERS-CoV, HCoV-OC43 and HCoV-299E, under 17
312 temperature-RH conditions. We generated estimates of half-life and uncertainties (Extended
313 Data Table 2) and compared those estimates to the half-lives predicted by the mechanistic model
314 parametrized from our SARS-CoV-2 data. As data on evaporation kinetics were not available,
315 we estimated a unique half-life for each experimental condition, covering both the evaporation
316 and quasi-equilibrium phases. As virus decay during the evaporation phase is expected to be
317 minimal, and the evaporation phase to be short, the estimated half-life can be used as a proxy
318 for the quasi-equilibrium half-life. The complete data selection, extraction and analysis process
319 is detailed in the SI (section 3).

320 We also included data from SARS-CoV-1 and MERS-CoV collected by our group during
321 previous studies¹¹. Those data were collected at 22 °C and 40 % on polypropylene using the
322 protocol described previously¹¹ and similar to the one used to collect the SARS-CoV-2 data.
323 SARS-CoV-1 strain Tor2 (AY274119.3)⁵⁴ and MERS-CoV strain HCoV-EMC/2012⁵⁵ were
324 used for these experiments. We calculated half-lives for evaporation and quasi-equilibrium
325 phases using the same analysis pipeline used for SARS-CoV-2 (SI section 2.4). These data
326 were used only for out-of-sample prediction testing. We used the obtained evaporation phase
327 half-lives as proxies for the half-life at 100 % RH, as with SARS-CoV-2. See SI section 3.3 for
328 a figure showing model fits (Fig. S22) and a table of estimated half-lives (Table S1).

329 **Visualization**

330 We created plots in R using ggplot2⁵⁶, ggdist⁵⁷, and tidybayes⁵⁸, and created original
331 schematics using BioRender.com.

332 **References**

- 333 1. Marr, L. C., Tang, J. W., Van Mullekom, J. & Lakdawala, S. S. Mechanistic insights into
334 the effect of humidity on airborne influenza virus survival, transmission and incidence.
335 *Journal of the Royal Society Interface* **16**, 20180298 (2019).
- 336 2. Escudero, B., Rawsthorne, H., Gensel, C. & Jaykus, L. Persistence and transferability of
337 noroviruses on and between common surfaces and foods. *Journal of food protection* **75**,
338 927–935 (2012).
- 339 3. Ijaz, M. K., Brunner, A. H., Sattar, S. A., Nair, R. C. & Johnson-Lussenburg, C. M. Survival
340 Characteristics of Airborne Human Coronavirus 229E. *The Journal of General Virology*
341 **66** (Pt 12), 2743–2748. ISSN: 0022-1317 (Dec. 1985).
- 342 4. Chan, K.-H. *et al.* The effects of temperature and relative humidity on the viability of the
343 SARS coronavirus. *Advances in virology* **2011** (2011).
- 344 5. Van Doremalen, N., Bushmaker, T. & Munster, V. Stability of Middle East Respiratory
345 Syndrome coronavirus (MERS-CoV) under different environmental conditions. *Euro-
346 surveillance* **18**, 20590 (2013).
- 347 6. Biryukov, J. *et al.* Increasing Temperature and Relative Humidity Accelerates Inactivation
348 of SARS-CoV-2 on Surfaces. *Mosphere* **5** (2020).
- 349 7. Matson, M. J. *et al.* Effect of Environmental Conditions on SARS-CoV-2 Stability in
350 Human Nasal Mucus and Sputum. *Emerging Infectious Diseases* **26**, in press (2020).
- 351 8. Guillier, L. *et al.* Modelling the thermal inactivation of viruses from the Coronaviridae
352 family in suspensions or on surfaces with various relative humidities. *medRxiv* (2020).
- 353 9. Posada, J., Redrow, J. & Celik, I. A mathematical model for predicting the viability of
354 airborne viruses. *Journal of virological methods* **164**, 88–95 (2010).
- 355 10. Lin, K. & Marr, L. C. Humidity-dependent decay of viruses, but not bacteria, in aerosols
356 and droplets follows disinfection kinetics. *Environmental Science & Technology* **54**, 1024–
357 1032 (2020).
- 358 11. Van Doremalen, N. *et al.* Aerosol and surface stability of SARS-CoV-2 as compared with
359 SARS-CoV-1. *New England Journal of Medicine* **382**, 1564–1567 (2020).
- 360 12. Adams, M. H. The stability of bacterial viruses in solutions of salts. *The Journal of general
361 physiology* **32**, 579 (1949).
- 362 13. Yap, T. F., Liu, Z., Shveda, R. A. & Preston, D. A Predictive Model of the Temperature-
363 Dependent Inactivation of Coronaviruses (2020).

- 364 14. Cavaliere, F., Masieri, S., Vagnoni, S., Proietti, R. & Magalini, S. I. Airway secretion
365 electrolytes: reflection of water and salt states of the body. *Critical care medicine* **17**,
366 891–894 (1989).
- 367 15. Dulbecco, R. & Freeman, G. Plaque production by the polyoma virus. *Virology* **8**, 396
368 (1959).
- 369 16. Yang, W. & Marr, L. C. Mechanisms by Which Ambient Humidity May Affect Viruses in
370 Aerosols. *Applied and Environmental Microbiology* **78**, 6781–6788 (2012).
- 371 17. Yang, W., Elankumaran, S. & Marr, L. C. Relationship between Humidity and Influenza
372 A Viability in Droplets and Implications for Influenza's Seasonality. *PloS ONE* **7** (2012).
- 373 18. Mikhailov, E., Vlasenko, S., Niessner, R. & Pöschl, U. Interaction of aerosol particles
374 composed of protein and saltswith water vapor: hygroscopic growth and microstructural
375 rearrangement (2004).
- 376 19. Casanova, L. M., Jeon, S., Rutala, W. A., Weber, D. J. & Sobsey, M. D. Effects of
377 air temperature and relative humidity on coronavirus survival on surfaces. *Applied and*
378 *environmental microbiology* **76**, 2712–2717 (2010).
- 379 20. Songer, J. R. Influence of relative humidity on the survival of some airborne viruses.
380 *Applied microbiology* **15**, 35–42 (1967).
- 381 21. Johnson, G. *et al.* Modality of Human Expired Aerosol Size Distributions. *Journal of*
382 *Aerosol Science* **42**, 839–851. ISSN: 00218502 (Dec. 2011).
- 383 22. Johnson, D., Lynch, R., Marshall, C., Mead, K. & Hirst, D. Aerosol Generation by Modern
384 Flush Toilets. *Aerosol Science and Technology* **47**, 1047–1057. ISSN: 0278-6826 (Sept. 1,
385 2013).
- 386 23. Thompson, K.-A. *et al.* Influenza Aerosols in UK Hospitals during the H1N1 (2009)
387 Pandemic – The Risk of Aerosol Generation during Medical Procedures. *PLOS ONE* **8**,
388 e56278. ISSN: 1932-6203 (Feb. 13, 2013).
- 389 24. Chin, A. W. H. *et al.* Stability of SARS-CoV-2 in different environmental conditions. *The*
390 *Lancet Microbe* **1**, e10 (2020).
- 391 25. Chin, A. W. H. personal communication. Aug. 5, 2020.
- 392 26. Gamble, A. *et al.* Heat-treated virus inactivation rate depends strongly on treatment pro-
393 cedure. *bioRxiv* (2020).
- 394 27. Leclerc, Q. J. *et al.* What Settings Have Been Linked to SARS-CoV-2 Transmission
395 Clusters? *Wellcome Open Research* **5**, 83. ISSN: 2398-502X (June 5, 2020).

- 396 28. Dyal, J. W. COVID-19 Among Workers in Meat and Poultry Processing Facilities — 19
397 States, April 2020. *Morbidity and Mortality Weekly Report* **69** (2020).
- 398 29. Günther, T. *et al.* Investigation of a superspreading event preceding the largest meat pro-
399 cessing plant-related SARS-CoV-2 outbreak in Germany. *SSRN* (2020).
- 400 30. Khanh, N. C. *et al.* Transmission of Severe Acute Respiratory Syndrome Coronavirus 2
401 During Long Flight. *Emerging Infectious Diseases* (2020).
- 402 31. Jayaweera, M., Perera, H., Gunawardana, B. & Manatunge, J. Transmission of COVID-19
403 virus by droplets and aerosols: A critical review on the unresolved dichotomy. *Environ-
404 mental Research*, 109819 (2020).
- 405 32. Seyer, A. & Sanlidag, T. Solar ultraviolet radiation sensitivity of SARS-CoV-2. *The Lancet
406 Microbe* **1**, e8–e9 (2020).
- 407 33. Kormuth, K. A. *et al.* Influenza virus infectivity is retained in aerosols and droplets
408 independent of relative humidity. *The Journal of infectious diseases* **218**, 739–747 (2018).
- 409 34. Prussin, A. J. *et al.* Survival of the enveloped virus Phi6 in droplets as a function of relative
410 humidity, absolute humidity, and temperature. *Applied and environmental microbiology*
411 **84** (2018).
- 412 35. Benbough, J. E. Some factors affecting the survival of airborne viruses. *The Journal of
413 General Virology* **10**, 209–220 (1971).
- 414 36. Asadi, S. *et al.* Influenza A Virus Is Transmissible via Aerosolized Fomites. *Nature Com-
415 munications* **11**, 4062. ISSN: 2041-1723 (Aug. 18, 2020).
- 416 37. Ong, S. W. X. *et al.* Air, Surface Environmental, and Personal Protective Equipment
417 Contamination by Severe Acute Respiratory Syndrome Coronavirus 2 (SARS-CoV-2)
418 From a Symptomatic Patient. *JAMA* (Mar. 4, 2020).
- 419 38. Cai, J. *et al.* Indirect Virus Transmission in Cluster of COVID-19 Cases, Wenzhou, China,
420 2020. *Emerging Infectious Diseases* **26** (2020).
- 421 39. Fisher, D., Reilly, A., Zheng, A. K. E., Cook, A. R. & Anderson, D. Seeding of outbreaks
422 of COVID-19 by contaminated fresh and frozen food. *bioRxiv* (2020).
- 423 40. Kissler, S. M., Tedijanto, C., Goldstein, E., Grad, Y. H. & Lipsitch, M. Projecting the
424 transmission dynamics of SARS-CoV-2 through the postpandemic period. *Science*. ISSN:
425 0036-8075, 1095-9203. <https://science.sciencemag.org/content/early/2020/04/14/science.abb5793> (2020).
- 426 41. Baker, R. E., Yang, W., Vecchi, G. A., Metcalf, C. J. E. & Grenfell, B. T. Susceptible
427 supply limits the role of climate in the early SARS-CoV-2 pandemic. *Science* (2020).

- 429 42. Lofgren, E., Fefferman, N. H., Naumov, Y. N., Gorski, J. & Naumova, E. N. Influenza
430 Seasonality: Underlying Causes and Modeling Theories. *Journal of Virology* **81**, 5429–
431 5436. ISSN: 0022-538X, 1098-5514 (2007).
- 432 43. Carlson, C. J., Gomez, A. C., Bansal, S. & Ryan, S. J. Misconceptions about weather
433 and seasonality must not misguide COVID-19 response. *Nature Communications* **11**, 1–4
434 (2020).
- 435 44. Poirier, C. *et al.* The Role of Environmental Factors on Transmission Rates of the COVID-
436 19 Outbreak: An Initial Assessment in Two Spatial Scales. en. *Scientific Reports* **10**, 17002.
437 ISSN: 2045-2322 (Oct. 2020).
- 438 45. Onishi, K. G. *et al.* Circadian and circannual timescales interact to generate seasonal
439 changes in immune function. *Brain, Behavior, and Immunity* **83**, 33–43 (2020).
- 440 46. Shaman, J., Pitzer, V. E., Viboud, C., Grenfell, B. T. & Lipsitch, M. Absolute Humidity
441 and the Seasonal Onset of Influenza in the Continental United States. *PLoS Biology* **8**,
442 e1000316. ISSN: 1545-7885 (2010).
- 443 47. Webb, S., Bather, R. & Hodges, R. The effect of relative humidity and inositol on air-borne
444 viruses. *Canadian Journal of Microbiology* **9**, 87–92 (1963).
- 445 48. De Jong, J. & Winkler, K. The inactivation of poliovirus in aerosols. *Epidemiology &*
446 *Infection* **66**, 557–565 (1968).
- 447 49. Wigginton, K. R., Pecson, B. M., Sigstam, T., Bosshard, F. & Kohn, T. Virus inactivation
448 mechanisms: impact of disinfectants on virus function and structural integrity. *Environmental*
449 *Science & Technology* **46**, 12069–12078. ISSN: 1520-5851 (2012).
- 450 50. Holshue, M. L. *et al.* First Case of 2019 Novel Coronavirus in the United States. *New*
451 *England Journal of Medicine* **382**, 929–936 (2020).
- 452 51. Fischer, R. *et al.* Assessment of N95 respirator decontamination and re-use for SARS-
453 CoV-2. *Emerging Infectious Diseases* **In press** (2020).
- 454 52. Team, S. D. *The Stan Core Library* Version 2.18.0. 2018. <https://mc-stan.org/>.
- 455 53. Stan Development Team. RStan: the R interface to Stan. *R package version* **2** (2016).
- 456 54. Marra, M. A. *et al.* The genome sequence of the SARS-associated coronavirus. *Science*
457 **300**, 1399–1404 (2003).
- 458 55. Zaki, A. M., Van Boheemen, S., Bestebroer, T. M., Osterhaus, A. D. & Fouchier, R. A.
459 Isolation of a novel coronavirus from a man with pneumonia in Saudi Arabia. *New England*
460 *Journal of Medicine* **367**, 1814–1820 (2012).

- 461 56. Wickham, H. *ggplot2: Elegant Graphics for Data Analysis* ISBN: 978-3-319-24277-4.
462 <https://ggplot2.tidyverse.org> (Springer-Verlag New York, 2016).
- 463 57. Kay, M. *ggdist: Visualizations of Distributions and Uncertainty* R package version 2.2.0
464 (2020). <http://mjskay.github.io/ggdist/>.
- 465 58. Kay, M. *tidybayes: Tidy Data and Geoms for Bayesian Models* R package version 2.1.1
466 (2020). <http://mjskay.github.io/tidybayes/>.

Acknowledgements

This research was supported by the Intramural Research Program of the National Institute of Allergy and Infectious Diseases (NIAID), National Institutes of Health (NIH). JOL-S and AG were supported by the Defense Advanced Research Projects Agency DARPA PREEMPT #D18AC00031 and the UCLA AIDS Institute and Charity Treks, and JOL-S was supported by the U.S. National Science Foundation (DEB-1557022), the Strategic Environmental Research and Development Program (SERDP, RC-2635) of the U.S. QS, LCM, and PJV were supported by the U.S. National Science Foundation (CBET-1705653, CBET-2029911). The content of the article does not necessarily reflect the position or the policy of the U.S. government, and no official endorsement should be inferred.

Author contributions

VJM and JOL-S conceived the study. KCY performed the inactivation experiments, with support from TB, RJF, MJM, NvD, and VJM. QH performed the evaporation experiments, with support from PJV and LCM. DHM developed the mechanistic model and conducted statistical and theoretical analysis, with support from JOL-S, AG, FWR, and LCM. DHM wrote analysis code and produced figures and schematics. AG reviewed the literature on coronavirus stability and compiled and prepared data for meta-analysis. DHM and AG wrote the first draft of the paper, which all authors edited.

Competing interests

We have no competing interests to declare.

Additional information

Supplementary Information

Supplementary information for this paper is available online.

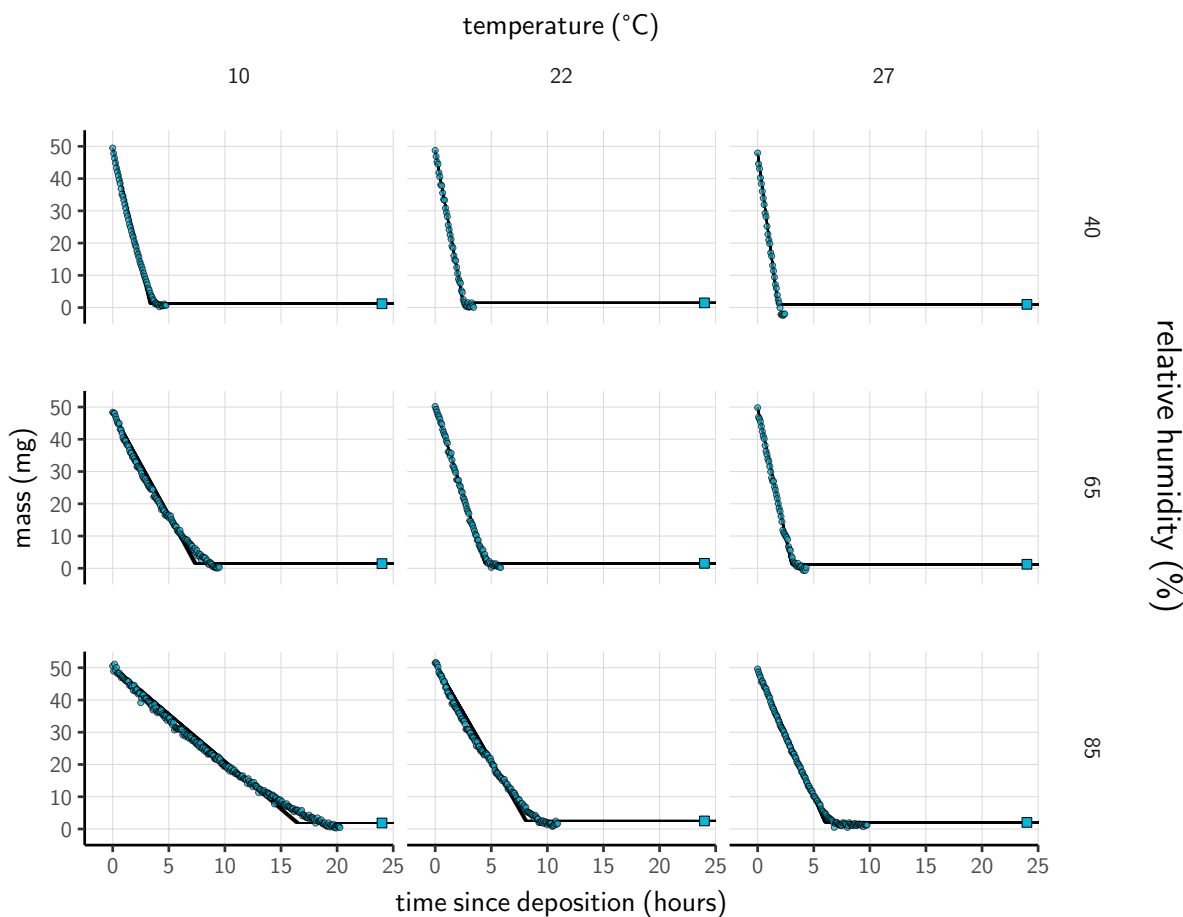
490 **Correspondence**

491 Correspondence and requests for materials should be addressed to Dylan H. Morris: dhmorris@princeton.edu.

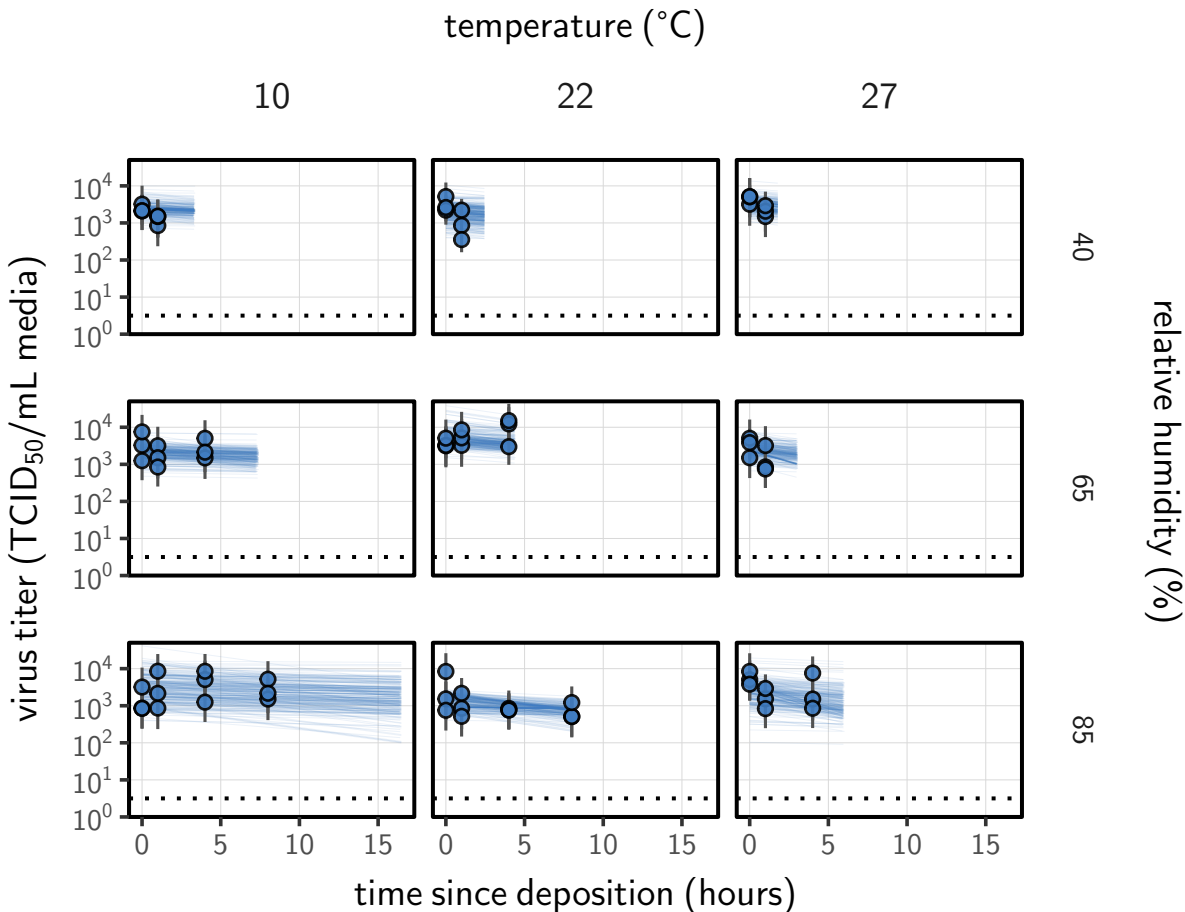
493 **Data availability**

494 All code and data needed to reproduce results and figures is archived on Github (<https://github.com/dylanhmorris/sars-cov-2-temp-humidity/>) and on Zenodo (<https://doi.org/10.5281/zenodo.4093265>), and licensed for reuse, with appropriate attribution/citation, under a BSD 3-Clause Revised License.

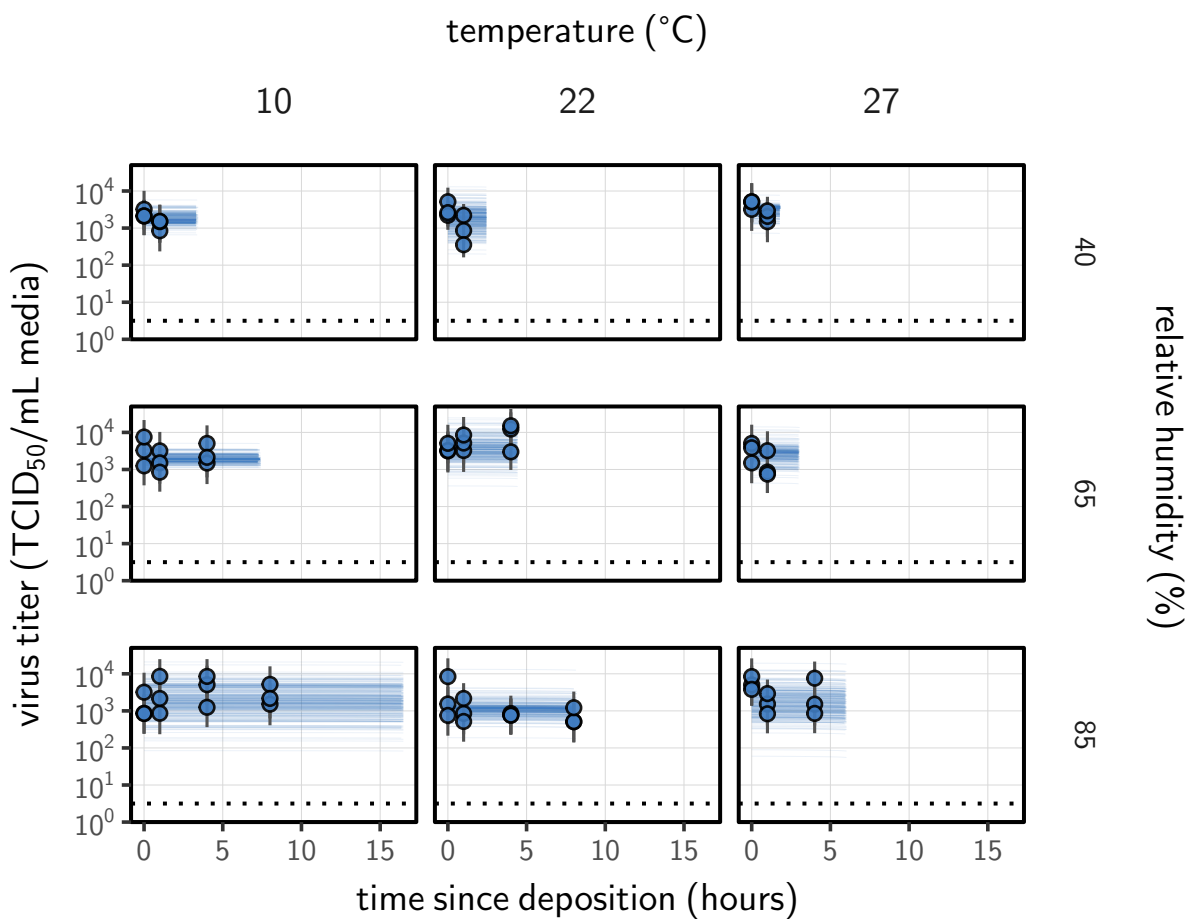
498 **Extended data figures**



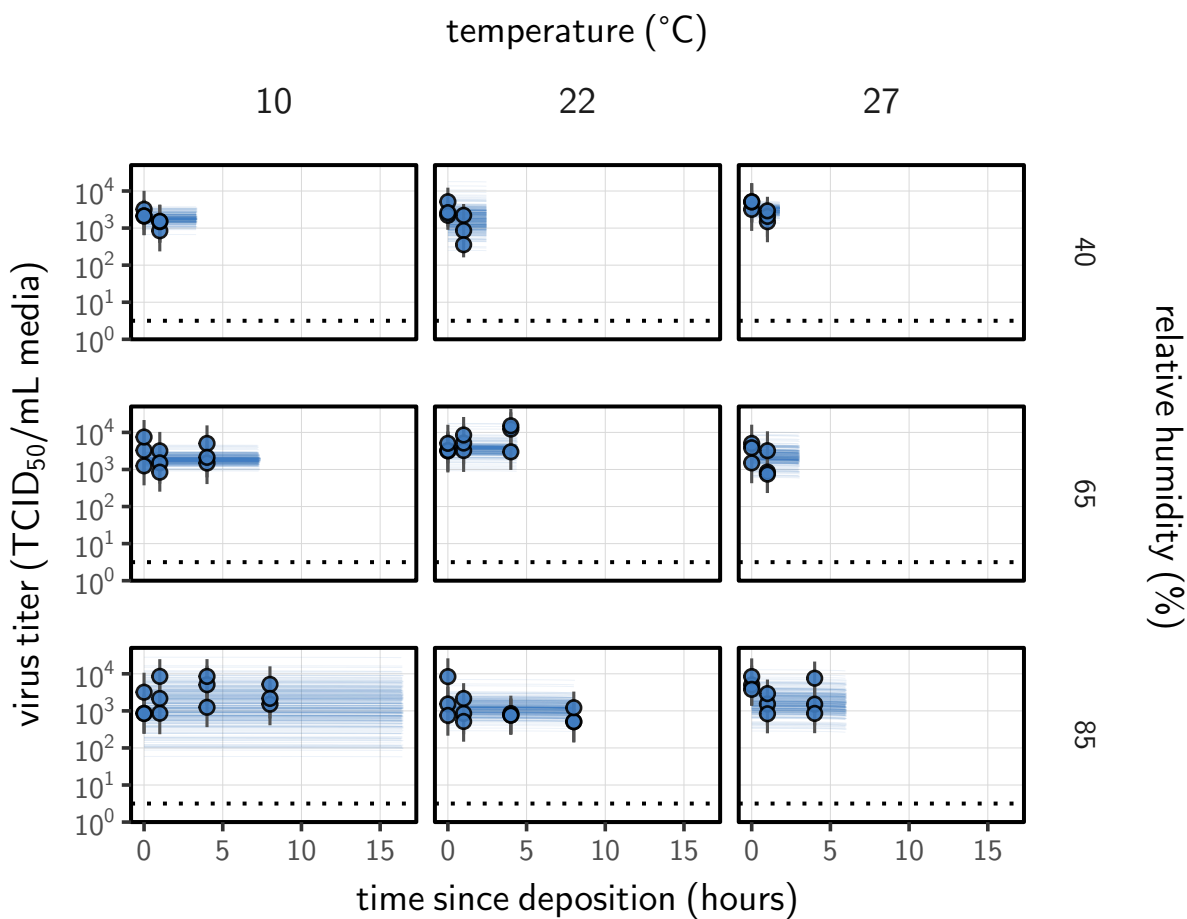
Extended Data Fig. 1 | Evaporation of supplemented Dulbecco's Modified Eagle Medium (DMEM) as a function of temperature and humidity. Dots show measured masses. Square shows measured final (quasi-equilibrium) mass; actual measurement times for final masses were upon removal of sample from chamber, but for readability they are plotted at 24 h for all experiments. Lines are 100 random draws from the posterior for the evaporation rate; horizontal section of line reflects the reaching of quasi-equilibrium (measured final mass). Transition point between evaporation phase and quasi-equilibrium phase inferred from data (see SI sections 1.2, 2.3). Note that final mass measurement is more accurate than timeseries measurements (see the [Evaporation experiment](#) subsection of the [Methods](#))



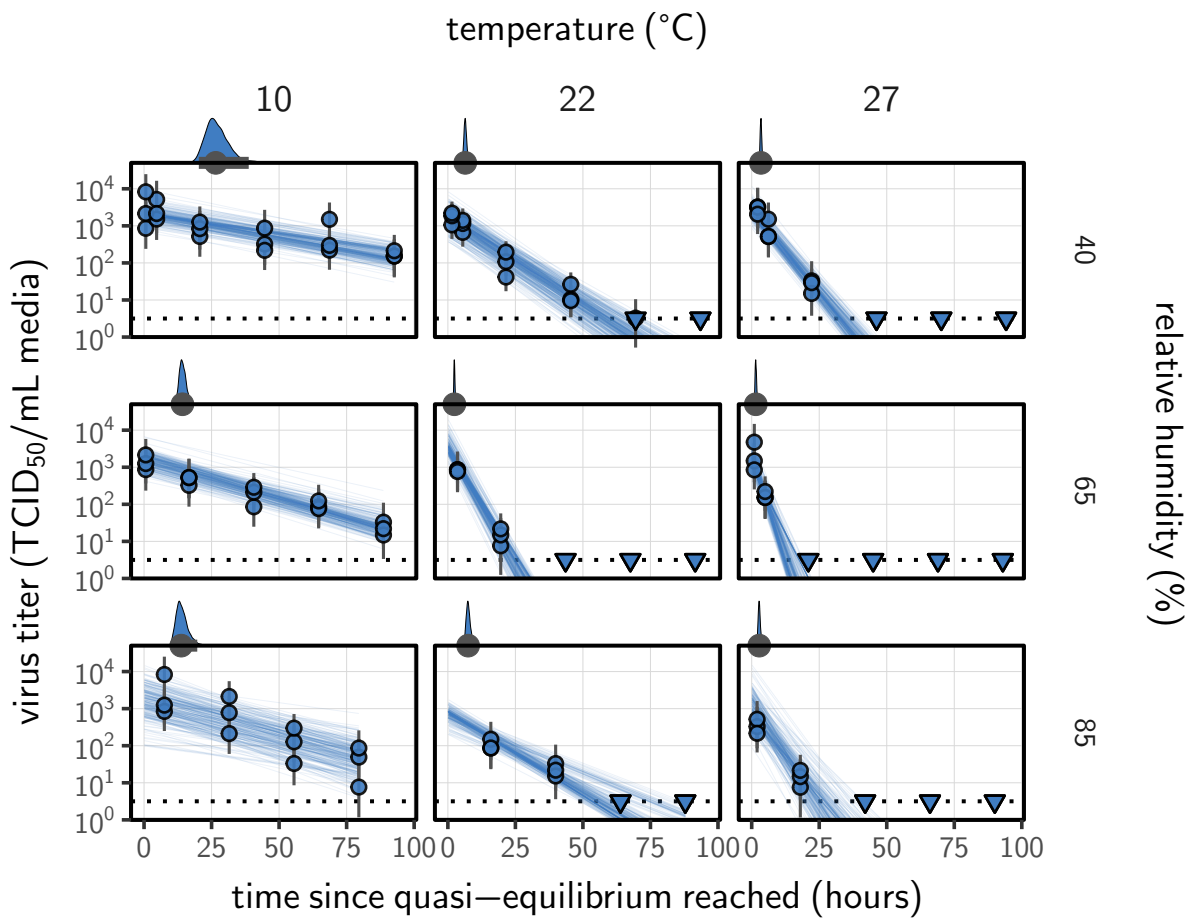
Extended Data Fig. 2 | Fit of the simple regression model to the evaporation phase (pre-drying) SARS-CoV-2 titer data. Points show posterior median estimated titers in \log_{10} TCID₅₀/mL for each sample; lines show 95 % credible intervals. Time-points with no positive wells for any replicate are plotted as triangles at the approximate single-replicate limit of detection (LOD) of the assay—denoted by a black dotted line at $10^{0.5}$ TCID₅₀/mL media—to indicate that a range of sub-LOD values are plausible. Three samples collected at each time-point. x-axis shows time since sample deposition. Lines are truncated at the estimated time quasi-equilibrium was reached. Lines are random draws (10 per sample) from the joint posterior distribution of the initial sample virus concentration and the estimated decay rate; the distribution of lines gives an estimate of the uncertainty in the decay rate and the variability of the initial titer for each experiment.



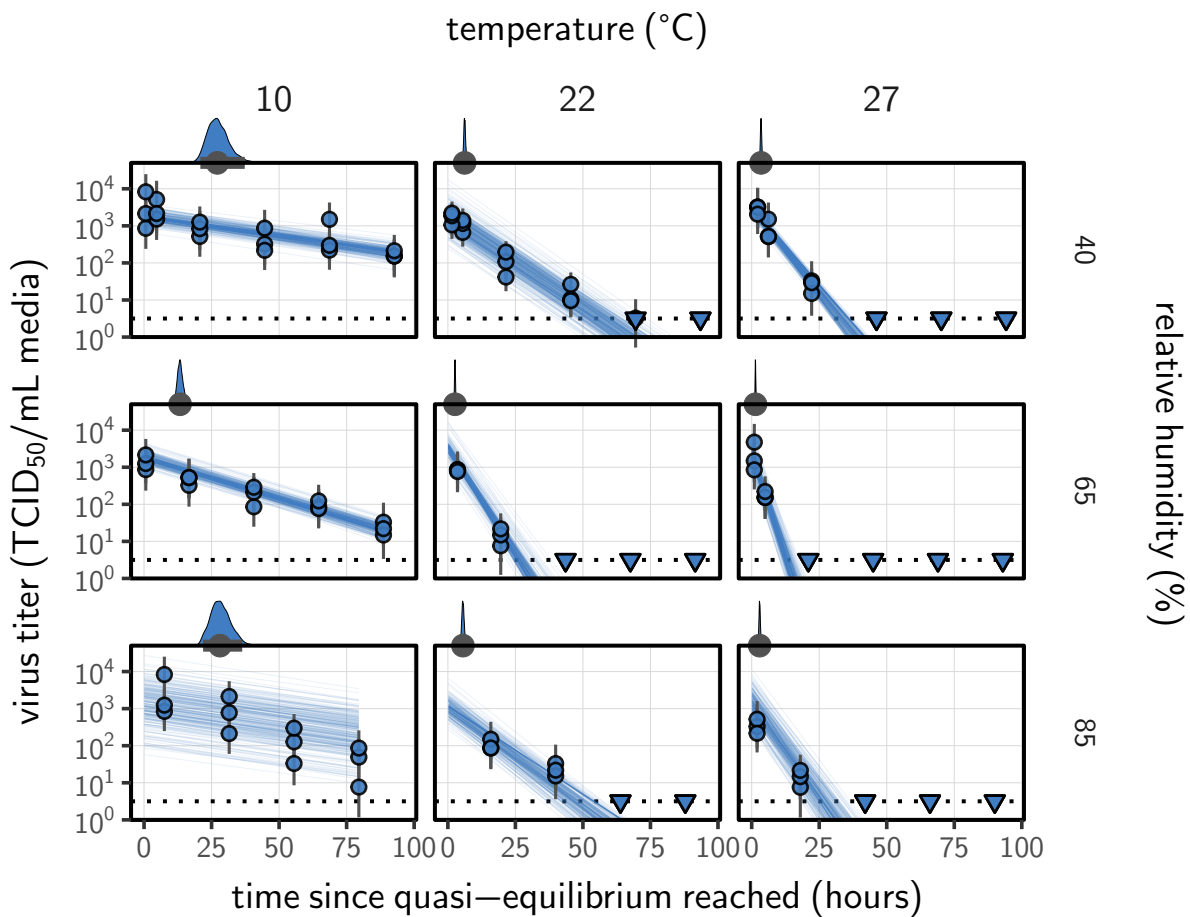
Extended Data Fig. 3 | Estimated titers and measured concentration model fit for SARS-CoV-2 stability on plastic during the evaporation phase. Points show posterior median estimated titers in $\log_{10}\text{TCID}_{50}/\text{mL}$ for each sample; lines show 95 % credible intervals. Time-points with no positive wells for any replicate are plotted as triangles at the approximate single-replicate limit of detection (LOD) of the assay—denoted by a black dotted line at $10^{0.5} \text{ TCID}_{50}/\text{mL media}$ —to indicate that a range of sub-LOD values are plausible. Three samples collected at each time-point. x-axis shows time since sample deposition. Lines are truncated at the estimated time quasi-equilibrium was reached. Lines are random draws (10 per sample) from the joint posterior distribution of the initial sample virus concentration and the mechanistic model predicted decay rate; the distribution of lines gives an estimate of the uncertainty in the decay rate and the variability of the initial titer for each experiment.



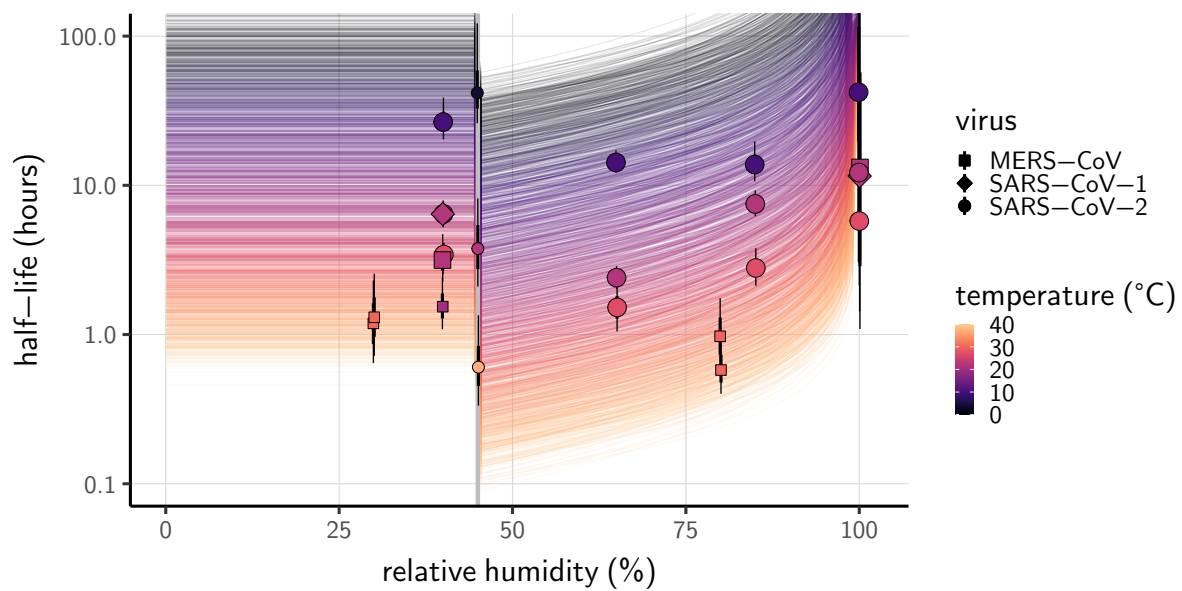
Extended Data Fig. 4 | Estimated titers and modeled concentration model fit for SARS-CoV-2 stability on plastic during the evaporation phase. Points show posterior median estimated titers in \log_{10} TCID₅₀/mL for each sample; lines show 95 % credible intervals. Time-points with no positive wells for any replicate are plotted as triangles at the approximate single-replicate limit of detection (LOD) of the assay—denoted by a black dotted line at $10^{0.5}$ TCID₅₀/mL media—to indicate that a range of sub-LOD values are plausible. Three samples collected at each time-point. x-axis shows time since sample deposition. Lines are truncated at the estimated time quasi-equilibrium was reached. Lines are random draws (10 per sample) from the joint posterior distribution of the initial sample virus concentration and the mechanistic model predicted decay rate; the distribution of lines gives an estimate of the uncertainty in the decay rate and the variability of the initial titer for each experiment.



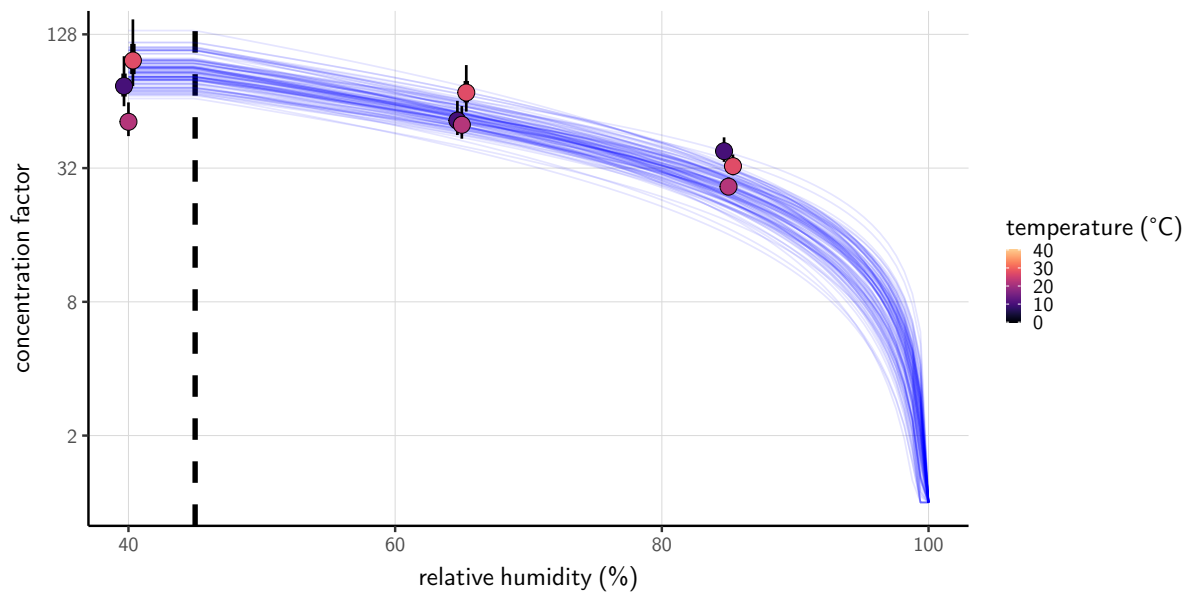
Extended Data Fig. 5 | Fit of the simple regression model to the quasi-equilibrium (post-drying) SARS-CoV-2 titer data. Points show posterior median estimated titers in $\log_{10} \text{TCID}_{50}/\text{mL}$ for each sample; lines show 95 % credible intervals. Time-points with no positive wells for any replicate are plotted as triangles at the approximate single-replicate limit of detection (LOD) of the assay—denoted by a black dotted line at $10^{0.5} \text{ TCID}_{50}/\text{mL}$ media—to indicate that a range of sub-LOD values are plausible. Three samples collected at each time-point. x-axis shows time since quasi-equilibrium was reached, as measured in evaporation experiments. Lines are random draws (10 per sample) from the joint posterior distribution of the initial sample virus concentration and the estimated decay rate; the distribution of lines gives an estimate of the uncertainty in the decay rate and the variability of the initial titer for each experiment. Density plots above each box show posterior distribution of virus half-life according to the model for the given condition; point under the density shows the posterior median half-life and line shows a 95 % credible interval.



Extended Data Fig. 6 | Estimated titers and modeled concentration model fit for SARS-CoV-2 stability on plastic at quasi-equilibrium. Points show posterior median estimated titers in $\log_{10} \text{TCID}_{50}/\text{mL}$ for each sample; lines show 95 % credible intervals. Time-points with no positive wells for any replicate are plotted as triangles at the approximate single-replicate limit of detection (LOD) of the assay—denoted by a black dotted line at $10^{0.5} \text{ TCID}_{50}/\text{mL}$ media—to indicate that a range of sub-LOD values are plausible. Three samples collected at each time-point. x-axis shows time since quasi-equilibrium was reached, as measured in evaporation experiments. Lines are random draws (10 per sample) from the joint posterior distribution of the initial sample virus concentration and the mechanistic model predicted decay rate; the distribution of lines gives an estimate of the uncertainty in the decay rate and the variability of the initial titer for each experiment. Density plots above each box show posterior distribution of virus half-life according to the model for the given condition; point under the density shows the posterior median half-life and line shows a 95 % credible interval.



Extended Data Fig. 7 | Modeled concentration fit predictions compared to half-lives estimated directly from data. Lines show half-life as a function of relative humidity (x-axis value) and temperature (color) according to the modeled concentration fit. 100 random draws from the posterior distribution are plotted for each of 20 evenly spaced temperatures between 0 and 40°C. Points show posterior median for measured half-lives for human coronaviruses from our study and from the literature (Extended Data Table 2); lines show a 68 % (thick) and 95 % (thin) credible interval. Half-lives estimates are model-free (i.e. no mechanistic model; fitting of independent exponential decay rates to each condition). Shape indicates virus; measurements from our own group are shown slightly larger. Estimated evaporation phase half-lives plotted at 100 % relative humidity (RH). Grey line shows the efflorescence relative humidity (ERH), 45 %.



Extended Data Fig. 8 | Concentration factor at quasi-equilibrium as a function of relative humidity, modeled concentration fit. Points show estimates for quasi-equilibrium concentration factor based on empirically measured masses from the evaporation experiments (Extended Data Fig. 1) and the estimated initial solute mass fraction from the modeled concentration fit (see Main Text, [Methods](#)). Estimates shown for each temperature (point color) and ambient RH (x-axis value). Vertical lines around the points show a 68 % (thick) and 95 % (thin) credible interval. Blue curves show model predictions for concentration factor given parameters α_c , α_s (Supplementary Information section 1.1, equation 8), and the initial solute mass fraction, all estimated from the measured concentration fit. Each is an independent draw from the joint posterior distribution of the parameters, thus giving a sense of the distribution of possible curves. Vertical dashed line shows the efflorescence relative humidity, 45 %.

499 **Extended data tables**

Extended Data Table 1 | Estimated half-lives in hours of SARS-CoV-2 on polypropylene as a function of temperature (T) and relative humidity (RH). Estimated half-lives are reported as posterior median and the middle 95% credible interval.

	T (°C)	RH (%)	median half-life (h)	2.5 %	97.5 %
quasi-equilibrium phase	10	40		26.55	20.28
	10	65		14.22	12.17
	10	85		13.78	10.67
	22	40		6.43	5.52
	22	65		2.41	2.03
	22	85		7.50	6.22
	27	40		3.43	2.91
	27	65		1.52	1.05
	27	85		2.79	2.12
evaporation phase	10		42.08	10.97	334.34
	22		12.18	4.47	163.58
	27		5.76	2.14	125.85

Extended Data Table 2 | Estimated half-lives in hours for data from the literature, as a function of material, temperature (T), and relative humidity (RH). Estimated half-lives are reported as posterior median and the middle 95% credible interval. CCM: cell culture medium; VTM: virus transport medium; Resp. sec.: respiratory secretions

study	virus	material	T (°C)	RH (%)	median half-life (h)	2.5 %	97.5 %
Harbourt <i>et al.</i> 2020 ⁵⁹	SARS-CoV-2	Skin	4	45	4.17×10^1	2.61×10^1	1.22×10^2
Lamarre <i>et al.</i> 1989 ⁶⁰	HCov-229E	Bulk CCM	4		1.97×10^2	5.06×10^1	1.05×10^4
Rabenau <i>et al.</i> 2005 ⁶¹	SARS-CoV-1	Bulk CCM	4		1.24	1.18×10^{-1}	9.73×10^2
Lai <i>et al.</i> 2005 ⁶²	SARS-CoV-1	Bulk Resp. sec.	4		4.42×10^1	3.68×10^1	5.56×10^1
Chin <i>et al.</i> 2020 ²⁴	SARS-CoV-2	Bulk VTM	4		1.98×10^2	5.45×10^1	9.09×10^3
Van Doremalen <i>et al.</i> 2013 ⁵	MERS-CoV	Plastic	20	40	1.54	1.08	2.42
Van Doremalen <i>et al.</i> 2013 ⁵	MERS-CoV	Steel	20	40	3.14	2.26	4.71
Lai <i>et al.</i> 2005 ⁶²	SARS-CoV-1	Bulk Resp. sec.	20		1.10×10^1	8.45	1.61×10^1
Harbourt <i>et al.</i> 2020 ⁵⁹	SARS-CoV-2	Skin	22	45	3.77	2.10	8.17
Lamarre <i>et al.</i> 1989 ⁶⁰	HCov-229E	Bulk CCM	22		1.51×10^1	8.82	2.55×10^1
Chin <i>et al.</i> 2020 ²⁴	SARS-CoV-2	Bulk VTM	22		1.83×10^1	1.35×10^1	2.62×10^1
Van Doremalen <i>et al.</i> 2013 ⁵	MERS-CoV	Plastic	30	30	1.19	6.44×10^{-1}	2.31
Van Doremalen <i>et al.</i> 2013 ⁵	MERS-CoV	Steel	30	30	1.31	7.20×10^{-1}	2.56
Van Doremalen <i>et al.</i> 2013 ⁵	MERS-CoV	Plastic	30	80	9.73×10^{-1}	5.66×10^{-1}	1.75
Van Doremalen <i>et al.</i> 2013 ⁵	MERS-CoV	Steel	30	80	5.78×10^{-1}	4.01×10^{-1}	9.96×10^{-1}
Bucknall <i>et al.</i> 1972 ⁶³	HCov-229E	Bulk CCM	33		1.61	1.01	4.02
Bucknall <i>et al.</i> 1972 ⁶³	HCov-OC43	Bulk CCM	33		6.70	3.71	6.24×10^1
Lamarre <i>et al.</i> 1989 ⁶⁰	HCov-229E	Bulk CCM	33		1.42×10^1	8.68	2.27×10^1
Harbourt <i>et al.</i> 2020 ⁵⁹	SARS-CoV-2	Skin	37	45	6.05×10^{-1}	3.34×10^{-1}	1.35
Bucknall <i>et al.</i> 1972 ⁶³	HCov-229E	Bulk CCM	37		1.04	6.51×10^{-1}	2.06
Bucknall <i>et al.</i> 1972 ⁶³	HCov-OC43	Bulk CCM	37		4.19	2.34	4.03×10^1
Lamarre <i>et al.</i> 1989 ⁶⁰	HCov-229E	Bulk CCM	37		5.77	2.84	1.10×10^1
Chin <i>et al.</i> 2020 ²⁴	SARS-CoV-2	Bulk VTM	37		2.09	1.45	3.13
Batéjat <i>et al.</i> 2020 ⁶⁴	SARS-CoV-2	Bulk CCM	56		2.25×10^{-2}	1.66×10^{-2}	2.78×10^{-2}
Darnell <i>et al.</i> 2004 ⁶⁵	SARS-CoV-1	Bulk CCM	56		4.50×10^{-2}	3.41×10^{-2}	6.31×10^{-2}
Leclercq <i>et al.</i> 2014 ⁶⁶	MERS-CoV	Bulk CCM	56		4.31×10^{-3}	1.29×10^{-3}	1.51×10^{-2}
Rabenau <i>et al.</i> 2005 ⁶¹	SARS-CoV-1	Bulk CCM	56		3.38×10^{-3}	9.53×10^{-6}	2.63×10^{-2}
Chin <i>et al.</i> 2020 ²⁴	SARS-CoV-2	Bulk VTM	56		1.64×10^{-2}	1.09×10^{-2}	2.89×10^{-2}
Pagat <i>et al.</i> 2007 ⁶⁷	SARS-CoV-1	Bulk CCM	60		3.48×10^{-2}	2.59×10^{-2}	5.09×10^{-2}
Rabenau <i>et al.</i> 2005 ⁶¹	SARS-CoV-1	Bulk CCM	60		3.08×10^{-3}	1.18×10^{-5}	2.62×10^{-2}
Batéjat <i>et al.</i> 2020 ⁶⁴	SARS-CoV-2	Bulk CCM	65		1.56×10^{-3}	6.84×10^{-6}	1.17×10^{-2}
Darnell <i>et al.</i> 2004 ⁶⁵	SARS-CoV-1	Bulk CCM	65		4.13×10^{-2}	3.11×10^{-2}	6.26×10^{-2}
Leclercq <i>et al.</i> 2014 ⁶⁶	MERS-CoV	Bulk CCM	65		7.34×10^{-4}	5.15×10^{-4}	1.45×10^{-3}
Batéjat <i>et al.</i> 2020 ⁶⁴	SARS-CoV-2	Bulk Resp. sec.	65		8.38×10^{-3}	6.01×10^{-3}	1.15×10^{-2}
Pagat <i>et al.</i> 2007 ⁶⁷	SARS-CoV-1	Bulk CCM	70		9.82×10^{-3}	7.71×10^{-3}	1.40×10^{-2}
Chin <i>et al.</i> 2020 ²⁴	SARS-CoV-2	Bulk VTM	70		3.34×10^{-3}	1.66×10^{-3}	6.13×10^{-3}
Darnell <i>et al.</i> 2004 ⁶⁵	SARS-CoV-1	Bulk CCM	75		2.24×10^{-3}	9.48×10^{-6}	2.13×10^{-2}
Batéjat <i>et al.</i> 2020 ⁶⁴	SARS-CoV-2	Bulk Resp. sec.	95		2.42×10^{-3}	1.61×10^{-3}	3.62×10^{-3}